ACS SENSORS

pubs.acs.org/acssensors

Article

Microscale Biosensor Array Based on Flexible Polymeric Platform toward Lab-on-a-Needle: Real-Time Multiparameter Biomedical Assays on Curved Needle Surfaces

Jaeho Park,[§] Juliane R. Sempionatto,[§] Jayoung Kim, Yongrok Jeong, Jimin Gu, Joseph Wang,*[,§] and Inkyu Park*[,§]

Cite This: *ACS Sens.* 2020, 5, 1363−1373

Read Online

ACCESS | Metrics & More | Article Recommendations | Supporting Information

ABSTRACT: In vivo sensing of various physical/chemical parameters is gaining increased attention for early prediction and management of various diseases. However, there are major limitations on the fabrication method of multiparameter needle-based in vivo sensing devices, particularly concerning the uniformity between sensors. To address these challenges, we developed a microscale biosensor array for the measurement of electrical conductivity, pH, glucose, and lactate concentrations on a flexible polymeric polyimide platform with electrodeposited electrochemically active layers. The biosensor array was then transferred to a medical needle toward multiparametric in vivo sensing. The flexibility of the sensor platform allowed an easy integration to the curved surface (φ = 1.2 mm) of the needle. Furthermore, the electrodeposition process was used to localize various active materials for corresponding electrochemical sensors on the microscale electrodes with a high precision (patterning area = 150 μm × 2 mm). The biosensor array-modified needle was aimed to discriminate cancer from normal tissues by providing real-time discrimination of glucose, lactate concentration, pH, and electrical conductivity changes associated with the cancer-specific metabolic processes. The sensor performance was thus evaluated using solution samples, covering the physiological concentrations for cancer discrimination. Finally, the possibility of in vivo electrochemical biosensing during needle insertion was confirmed by utilizing the needle in a hydrogel phantom that mimicked the normal and cancer microenvironments.

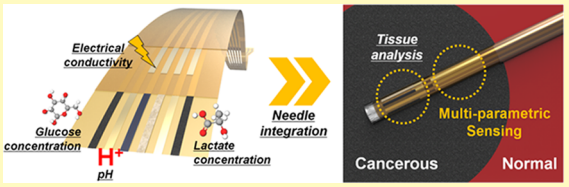

KEYWORDS: *multiparametric sensing, flexible electrochemical sensor, pH sensor, glucose sensor, lactate sensor, electrical conductivity sensor, in vivo sensing, lab-on-a-needle*

Enzyme-based electrochemical sensors have greatly evolved since they were first proposed by Clark and Lyons in the 1950s.[1] In the healthcare area, we have experienced the widespread use of electrochemical biosensors in centralized clinical tests, performed in controlled environments and laboratories, followed by point-of-care portable sensors, such as the glucose sensor strip introduced in the 1980s, and recent trends toward wearable and implantable electrochemical sensors capable of real-time on-body diagnosis. This evolution has brought us many advances toward the prevention, management, and treatment of diseases as well as new materials and technologies.[2−7] Important features of these modern sensors are the ability to conform to the body and various other curved surfaces and high integration of miniaturized multiparameter sensors. The development of microscale flexible electrochemical devices has allowed the rapid uprise of implantable sensors and sensor integrated medical devices, such as a medical wire, a medical needle, an endoscope, etc.[8−10] Implantable sensors are strong candidates for next-generation enzyme sensors, with glucose monitoring devices, employing implantable needles, receiving tremendous attention toward continuous blood glucose measurements. Needle devices with the capability of a bioassay for the disease diagnostic and management have been intensively explored recently.[8,11−13]

Functionalized needles can be used not only for the continuous sensing of analytes but also during medical procedures by integrating microscale sensors onto the medical tools used for surgery and medical treatment. This approach ensures a safer medical procedure by analyzing the tissue environment inside the patient's body. However, to perform the above-mentioned bioassay in an in vivo environment, it is essential that the electrochemical biosensors approach the target position or the target tissue in a minimally invasive manner. There have been reports about an in vivo bioassay based on the electrochemical sensor integrated within medical tools such as needle, endoscope, microwire, etc.[8−10] In general, to integrate the sensor onto the medical tool, the sensors have

Received: January 12, 2020
Accepted: February 13, 2020
Published: February 27, 2020

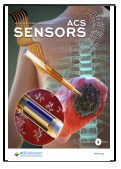

https://dx.doi.org/10.1021/acssensors.0c00078
ACS Sens. 2020, 5, 1363−1373

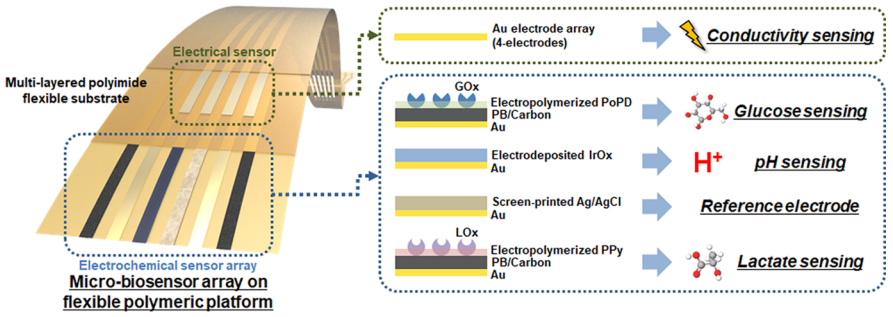

Figure 1. Schematics of the microbiosensor array on the flexible polymeric platform: the microbiosensor array with the capability of electrical sensing (electrical conductivity sensor) and electrochemical sensing (iridium oxide-based pH sensor, enzymatic glucose sensor, and enzymatic lactate sensor) is fabricated on the multilayered polyimide flexible substrate. The electrodeposition is carried out to form various active layers on each electrode with a dimension of 150 μm × 2 mm.

been directly fabricated using the needle or the microwire as an electrode itself, and functional materials for electrochemical sensors were coated on those surfaces by various deposition methods, such as screen printing, dip-coating, electrodeposition, winding functional wires on the surface, etc.[8,14−18] However, these approaches possess several limitations, including the uniformity between the sensors since the control of the line width and spacing between neighboring electrodes is very difficult using these methods. This lack of precision also prevents the development of multianalyte sensor arrays where various types of electrochemical sensors are integrated onto a single needle or wire. Besides the precise fabrication of multiple transducers onto a single medical tool, such multianalyte microdevices require selective patterning of the functional reagent materials onto the individual electrode surfaces.

An alternative methodology for the fabrication of microsensors for in vivo real-time analysis is the integration of flexible sensors, fabricated on the thin polymeric membrane or elastomeric membrane, to the needle or medical device. For example, Yu et al. developed a biopsy needle with the capability of sensing the tissue stiffness using an ultrasonic transceiver on a polyimide substrate.[11] The ultrasonic transceiver based on the lead zirconate titanate (PZT) was fabricated and transferred to the electrodes on the polyimide substrate with a thickness of about 3 μm. Then, the sensor was integrated on the surface of the biopsy needle with the PDMS interlayer for mechanical decoupling between the needle and the sensor. In addition to this work, several others were reported based on a similar approach.[8,19,20] In our previous report, we have developed a biopsy needle integrated with a multimodal physical/chemical sensor array with various electrochemical sensors by fabricating the sensors on the polymeric film and transferring them onto the surface of the needle.[8] Even though this approach allowed fine resolution of the electrode, there were still challenges in integrating the enzyme layer for the electrochemical sensor onto the microscale electrode. The drop-casting method, which is a general method for forming the enzyme layer, was utilized for the enzyme immobilization in our previous report, but size control of the drop-casted enzyme solution was extremely difficult, and the drop-casted enzyme solution could easily spread over neighboring electrodes. Therefore, it is not a suitable method for fabricating multiple microscale sensors with the distance between sensors being less than several hundreds of micrometers. To overcome this limitation, Du et al. utilized an electrohydrodynamic (EHD) jet printing to print the enzyme solution on the platinum (Pt) working electrode of the glucose sensor.[19] Although a high-resolution printing of the enzyme layer down to 30 μm was achievable, a high-cost alignment and printing systems were necessary. Thus, to ensure good performance of multiarray microsensors, an appropriate fabrication method and precise formation of the enzyme layer should be incorporated.

In this work, we report on the development of a microscale biosensor array on a flexible polyimide substrate with electrodeposited electrochemically active layers and integration onto a medical needle toward a real-time biomedical assay during a medical procedure. An array of six microscale electrodes, with 150 μm width and 150 μm spacing between them, was fabricated on a flexible polyimide membrane. Such fabrication of the biosensor electrode array was realized using micropatterning and screen printing technologies. The active layers for the electrochemical sensors, such as the metal oxide layer for the pH sensor, and the enzyme layers for glucose and lactate biosensors, were selectively deposited on each sensor electrode. A biosensor array for electrochemical sensing, containing three electrochemical sensors (pH, glucose, and lactate sensors) was fully integrated within a 2 mm × 2 mm area, while the whole sensing system, including the electrochemical and electrical sensors, were fully integrated within a 2 mm × 5 mm area (Figure 1). The fabricated microscale biosensor array was thin enough to be easily integrated into a 1.2 mm diameter needle with good conformal contact due to the low bending stiffness of the thin polyimide substrate. The medical needle integrated with the biosensor array was utilized for real-time tissue discrimination by performing a multiparametric bioassay. Specifically, we aimed to detect cancerous tissues by analyzing changes in different physical/chemical parameters in the microenvironment between normal and cancerous tissues. According to the previous reports, it is well known that there are significant differences in electrical conductivity, pH, glucose, and lactate concentrations between the microenvironments of the normal and cancerous tissues.[20−36] Such physical/chemical differences, associated with the cancer-specific metabolic processes, can thus be utilized as useful parameters for detecting cancer by distinguishing the abnormal disease tissue. The electrical conductivity of cancer is higher by several times to several orders than that of the normal tissue, although the reason is still not clear.[20,21,29−35] For the pH, the glucose, and the lactate concentrations, cancer has more acidic pH,[22−25,36] lower glucose concentration,[26,27] and higher lactate concentration[26,28] in the microenvironment in comparison to the

https://dx.doi.org/10.1021/acssensors.0c00078
ACS Sens. 2020, 5, 1363−1373

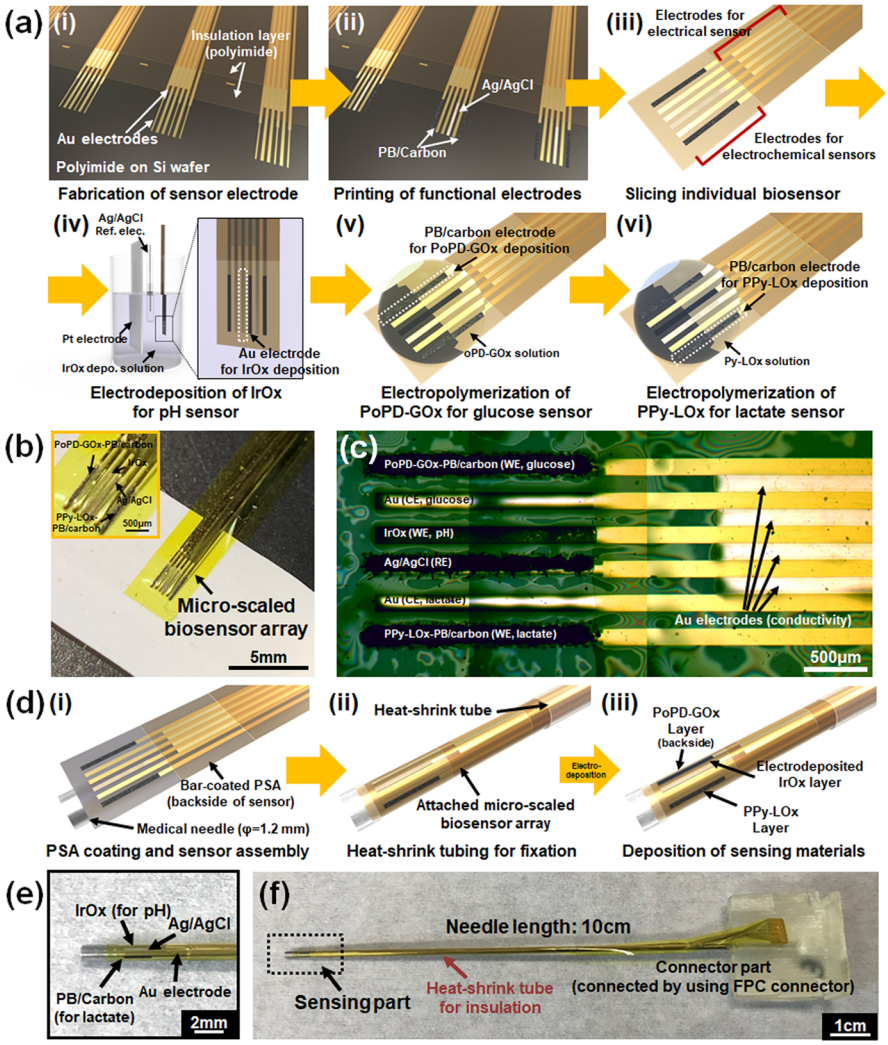

Figure 2. Schematic image of the fabrication process and photographs of fabrication results of (a–c) an on-plane-type microscale biosensor array and (d–f) the medical needle integrated with a biosensor array toward the lab-on-a-needle system: (a) schematic image of the fabrication process for the on-plane-type sensor. (b) Photograph of a fully fabricated and sliced microscale biosensor array. (c) Microscopic image of the sensing part of the biosensor array. (d) Schematic image of the integration process of the biosensor array onto the surface of the medical needle. (e) Magnified photograph of the sensing part. (f) Photograph of the biosensor array integrated medical needle toward a lab-on-a-needle system.

normal tissue as a result of the cancer-specific metabolic process (see Figure S1 for the schematic illustration about pH, glucose concentration, and lactate concentration in the cancer microenvironment). For the pH sensor, an electrodeposited iridium oxide (IrOx) layer was utilized as the active layer because of its high sensitivity, stable response, and biocompatibility.[37,38] The glucose and lactate electrochemical enzymatic biosensors relied on recognition by glucose oxidase (GOx) and lactate oxidase (LOx), respectively. The analytical characteristics of each sensor, which is integrated on the medical needle with a diameter of 1.2 mm, were quantitatively analyzed based on the solution sample that covers possible physiological ranges in both cancer and normal tissues. Then, the real-time multiparameter sensing ability was successfully demonstrated during the needle insertion into a cancer environment-mimicking hydrogel phantom.

■ EXPERIMENTAL SECTION

Materials and Chemicals. Polyimide varnish (VTEC PI-1388) for a polyimide film was purchased from Richard Blaine International Inc. (USA). The Prussian blue (PB)/carbon paste (C2070424P2) and Ag/AgCl paste (C2130102D1) were purchased from SunChemical (USA). Glucose oxidase and a lactate oxidase were supplied from Sigma-Aldrich (USA) and Toyobo (Japan), respectively. All other chemicals, such as iridium chloride hydrate ($IrCl_4 \cdot H_2O$), hydrogen peroxide solution (H_2O_2), oxalic acid ($(COOH)_2 \cdot 2H_2O$), potassium carbonate (K_2CO_3), *o*-phenylenediamine, sodium chloride (NaCl), D-(+)-glucose, lactic acid, monopotassium phosphate (KH_2PO_4), dipotassium phosphate (K_2HPO_4), and agarose powder were purchased from Sigma-Aldrich. A pressure-sensitive adhesive (MD7-4602) and a heat shrink tube were bought from Dow Corning (USA) and Nordson Medical (USA), respectively.

Design and Fabrication Process of the Au Sensor Electrode Array on the Flexible Substrate. Gold (Au) electrodes on the flexible polyimide substrate, for the sensor electrode array, as shown in Figure 2a-i, were fabricated using a conventional micropatterning technique (see also Figure S2 in the Supporting Information for the detailed fabrication process and structures). First, a polyimide film with a thickness of ~5 μm was formed on a 6 in. silicon wafer by spin-coating with a rotation speed of 3000 revolutions per minute (rpm), which was followed by the curing process in a convection oven at 150 °C for 30 min and 250 °C for 4 h sequentially. Then, Au electrodes (thickness of Ti/Au = 30/200 nm) for electrochemical sensors were fabricated using photolithography, electron beam evaporation, and the

https://dx.doi.org/10.1021/acssensors.0c00078
ACS Sens. 2020, 5, 1363–1373

lift-off process. The second polyimide film for the insulation of Au electrodes was formed by the same above-mentioned process. During the spin-coating process, the Kapton tape was attached at both end sides of the Au electrodes to avoid the insulation at the sensing part and the contact pad. Then, the second Au electrode layer (thickness of Ti/Au = 30/200 nm) for the electrical conductivity sensor and a final polyimide layer for the electrical insulation were fabricated by the same methods.

Screen Printing and Electrodeposition of Active Layers for Electrochemical Sensor. The PB/carbon electrode was used as a working electrode of both the glucose and the lactate sensors, and silver/silver chloride (Ag/AgCl) was used for the reference electrode. The reference and working electrodes were fabricated using the screen printing process. Patterns for the screen printing were designed in AutoCAD (Autodesk, USA) and transferred to a stainless steel mesh stencil supported by a steel frame (30 cm × 30 cm) (Daeshin Smartech, South Korea). The dimensions of the rectangular PB/carbon and Ag/AgCl electrodes were the same (150 μm × 2 mm). The electrodes were screen-printed in several steps. First, a PB/carbon paste was screen-printed on the gold traces for working electrodes of the glucose and lactate sensors and cured in a convection oven at 80 °C for 10 min, as shown in Figure 2c. Then, the Ag/AgCl paste was printed for the reference electrode followed by the curing process in the convection oven at 80 °C for 10 min (Figure 2c). After the screen printing process, the sensors were sliced individually using a razor blade, and the single sensor was handled for easier processing during electrodeposition of the active layers for the electrochemical sensors.

For the pH sensor, iridium oxide (IrOx) was used as the sensing material because of its high sensitivity, stable response, and biocompatibility.[37,38] The electrodeposition method was utilized to form the IrOx layer only at the exposed parts of the flexible Au electrode without electrical short between active materials on each Au electrode. The electrodeposition solution for the IrOx was prepared based on Yamanaka et al.'s work.[39] In brief, 50 mL of an aqueous solution containing 75 mg of iridium chloride solution, 0.5 mL of hydrogen peroxide solution (30 wt %), and 250 mg of oxalic acid was prepared, and the pH of the solution was tightly adjusted to 10.5 by adding potassium carbonate to the solution. The pH of solution was monitored using a commercial pH meter (PHB-550R, Omega, USA). Then, the prepared solution was stored in the dark space for at least 2 days for stabilization. For the electrodeposition, the sliced sensor, a platinized counter electrode, and a commercial Ag/AgCl reference electrode were immersed into the prepared solution (Figure 2a-iv) and cyclic voltammetry was performed. The potential range during the cyclic voltammetry was from −0.8 to 0.7 V, and it was performed for 100 cycles with a scan rate at 100 mV/s.

The immobilization of glucose oxidase (GOx) was performed through electropolymerization of *o*-phenylenediamine (oPD), as shown in Figure 2a-v. For the preparation of the electropolymerization solution, 10 mM oPD and 5 mM sodium sulfate were dissolved in pH 7.0 phosphate buffer saline (PBS) with a concentration of 0.1 M. Then, the solution was purged with nitrogen gas for 20 min to remove oxygen from the inside of the solution. During the nitrogen purging, a vial with the solution was covered with an aluminum foil to avoid light-induced polymerization. After the nitrogen purging, the GOx with a concentration of 1600 U/mL was dissolved into the solution. For the electropolymerization, 20 μL of the electropolymerization solution was dropped at the PB/carbon electrodes of the glucose sensor, and a constant potential of +0.55 V (vs screen-printed Ag/AgCl pseudo-reference electrode) was applied for 2 min. After the electropolymerization, the microbiosensor was immersed into the PBS for 20 min and further rinsed 10 times with a fresh PBS solution.

For the immobilization of lactate oxidase (LOx), the electropolymerization with pyrrole (Py) was carried out, as shown in Figure 2a-vi. For the electropolymerization solution, 4 mM pure pyrrole monomer, obtained through a vacuum distillation under 30 mbar at 70 °C, was dissolved into 0.1 M PBS solution with pH 7.4 followed by the dissolution of 600 U/mL LOx. For the electropolymerization, 20 μL of the electropolymerization solution was dropped on the PB/carbon electrode of the lactate sensor, and a constant potential of +0.8 V (vs screen-printed Ag/AgCl pseudo-reference electrode) was applied for 4 min. Then, the microbiosensor was rinsed with PBS by the same method for the glucose sensor.

Integration of the Flexible Microscale Biosensor Array onto the Surface of a Medical Needle. The fabricated microscale biosensor array on the flexible platform was integrated on the surface of a medical needle by attaching the biosensor without any electrodeposited active layers. First, a pressure-sensitive adhesive (PSA) was bar-coated on the backside of the microscale biosensor array to provide a temporal adhesion to the needle surface (Figure 2d-i). Then, the microscale biosensor array was conformally attached to the surface of the needle manually. However, the adhesion force with the temporary adhesion of PSA is not large enough to hold the microscale biosensor array, and it can be easily detached by shear force during the needle insertion. Therefore, to fix the biosensor array more tightly, the needle was covered using a polyethylene terephthalate (PET)-based heat shrink tube by heating with a heat gun at 110 °C. Then, the electrodeposition to form the active layers for electrochemical sensing was performed. The reason for the electrodeposition of active layers after the assembly of the microscale biosensor array is to avoid any unwanted damage or failure of the active layers. For example, the electrodeposited IrOx layer is too brittle to withstand the stress from mechanical bending after the fabrication process, and the enzyme layer can be damaged during heat shrink tubing. Except that the microscale biosensor array was on the surface of the needle, the protocols for the electrodeposition process were the same as the previously mentioned electrodeposition process.

Preparation of Solution Samples and Hydrogel Phantom for Sensor Characterization. For the characterization of the electrical conductivity sensor, saline solutions with sodium chloride (NaCl) were utilized. The conductivities of prepared saline solutions, covering human physiological range, were 0.0155, 0.0329, 0.0696, 0.1696, 0.447, and 1.096 S/m,[40−42] which were measured using a commercial conductivity meter (Orion Star A212, Thermo Fisher Scientific Inc., USA). Phosphate buffer solutions consisting of monopotassium phosphate (KH_2PO_4) and dipotassium phosphate (K_2HPO_4) were utilized to characterize the pH sensor. pH ranging from pH 6.6 to 7.4, which are possible physiological values in the human body,[22−24] was used. The pH was controlled by adjusting the molar ratio between KH_2PO_4 and K_2HPO_4. For the characterizations of the glucose and lactate sensors, a PBS containing D-(+)-glucose (0−4 mM) and lactic acid (0−6 mM) were utilized as the reference solutions, respectively. Such glucose and lactate concentration ranges were determined based on their variation in human normal and cancerous tissues.[26,27]

The hydrogel phantom for the real-time multiparameter sensing was made of agarose hydrogel. The hydrogel phantom consisted of a core−shell structure where the normal liver-mimicking region was the outer matrix and the liver cancer-mimicking region was the inner core, as shown in Figure 6a. The PBS solution used for the outer matrix had a similar physiological condition for the normal liver tissue (σ = 0.1243 S/m, pH 7.27, [glucose] = 2.5 mM, and [lactate] = 2.5 mM), while the PBS solution used for the inner core had a condition similar to that in the liver cancer (σ = 0.2315 S/m, pH 6.71, [glucose] = 1 mM, and [lactate] = 6 mM), according to previous works about the physiological conditions in normal and cancerous tissues.[26,34] To prepare the hydrogel phantom, first, 1 wt % agarose powder was dissolved on each prepared PBS solution by heating up the solution at 90 °C on a hot plate. Then, the fully mixed clear solution for the inner core was cooled down at room temperature, and the hydrogel was cut into a cube with dimensions of 1.2 cm × 1.2 cm × 1.2 cm. Next, the cut cube was wrapped with Parafilm to avoid diffusion of analytes to the outer matrix and placed inside the outer matrix agarose solution, which was cooled down at room temperature, while the inner core cube was hung inside the outer matrix.

Measurement System. An LCR meter (ZM-2410, NF Corporation, Japan) was used for the conductivity measurements of the electrical conductivity sensor. For the open-circuit potential

https://dx.doi.org/10.1021/acssensors.0c00078
ACS Sens. 2020, 5, 1363−1373

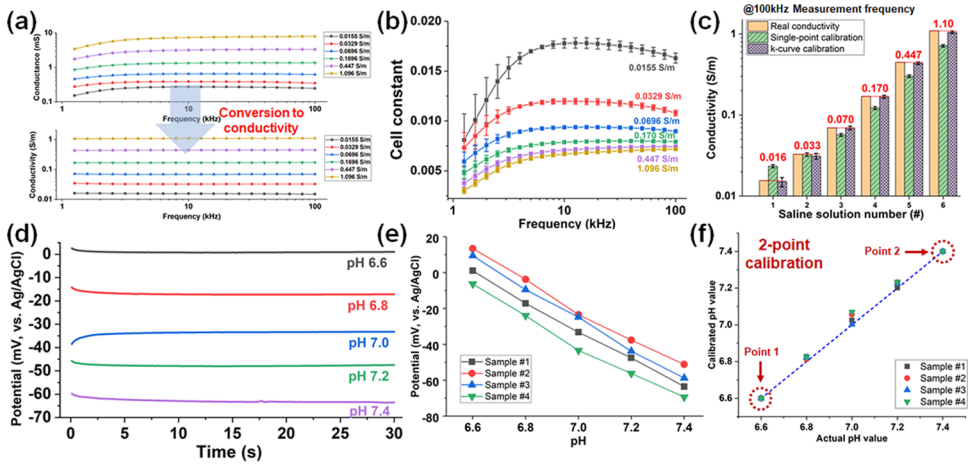

Figure 3. Characteristics of (a–c) the electrical conductivity sensor and (d–f) the IrOx-based pH sensor: (a) measured conductance and the converted conductivity in the conductivity range from 0.0155 to 1.096 S/m and the frequency range from 1 to 100 kHz. The conductivity was converted from the conductance data based on the calculated cell-constant curve (*k*-curve), which is shown in panel (b). (b) Average and standard deviation of the *k*-curves of the three electrical conductivity sensors. (c) Accuracy of the conversion process with three electrical conductivity sensors in the single-point and *k*-curve calibration at a frequency of 100 kHz. For the single-point calibration, a cell constant of one sensor at 0.0329 S/m was used, while the *k*-curve calibration used the *k*-curve of one sensor. (d) Measured OCP of the IrOx pH sensor for 30 s in the pH range from 6.6 to 7.4. (e) Calibration curves of four pH sensors in the pH range from 6.6 to 7.4. (f) Prediction plot between calibrated pH value and actual pH value. For the calibration, two-point calibration with the potential values at pH 6.6 and 7.4 was used.

measurements, cyclic voltammetry and chronoamperometry were performed using an electrochemical analyzer (CHI 6016D, CH Instrument, USA) for the characterization of electrochemical sensors. However, in the real-time multiparameter measurement with the hydrogel phantom, customized measurement systems including the LCR meter, an electrometer (6517A, Keithley, USA), a source meter (2400, Keithley, USA), and a switch module (34970a, 34904a, Agilent, USA) were constructed, as shown in Figure S3. In this customized system, the electrometer and the source meter were used instead of the electrochemical analyzer because of the synchronization of equipment in a single control LabVIEW program. Specifically, the switch module based on a mechanical relay was added to switch the connection between the sensor and the measurement equipment.

RESULTS AND DISCUSSION

Characterization of the Electrical Conductivity Sensor. The electrical conductivity is an intrinsic material property; however, the measurable parameter of the material from the LCR meter and the conductivity sensor is the electrical conductance, which is affected by the dimensional parameters of the sensor. Therefore, to obtain the conductivity from the measured conductance, the relation between the conductance and the conductivity is defined as a cell constant (k), and obtaining the cell constant before the conductivity measurement is an essential procedure in a commercial conductivity meter (see the detailed information about the cell constant in Section 1 in the Supporting Information). Thus, the cell constant of the electrical conductivity sensor on the microscale biosensor array was obtained and quantitatively analyzed by saline solutions. The saline solution is usually utilized for probe analysis because it is considered as a purely resistive component without a reactance term. Therefore, the measured conductance of the saline solution is constant, regardless of the frequency of the applied AC voltage, and the cell constant can be obtained as a constant value.[34,41]

The measured conductances of saline solutions, with conductivities from 0.0155 to 1.096 S/m and the frequencies from 1 to 100 kHz, are shown in Figure 3a. Although the measured conductance should be constant regardless of the frequency, the conductances for the frequency below 4 kHz tended to decrease for lower frequency. Furthermore, cell constants were also affected by the conductivity of the measured saline solution, as shown in Figure 3b. This can be attributed to the parasitic components from thin, long, and layered configuration of Au electrodes because the capacitance from Au electrodes can interfere with the AC current. Therefore, the conversion process from the measured conductance to the unknown conductivity should be able to compensate for the above-mentioned error induced from the parasitic component. To achieve this, we performed the cell constant curve (k-curve) calibration process as proposed in our previous work.[8,43] Instead of a single-point calibration process, which only utilizes a single cell constant from the sensor probe, the k-curve calibration process utilizes the cell constant as a function of the known conductivity of material and the used AC frequency. Based on the known k-curve and frequency used for the measurement, the unknown conductivity of the material can be calculated by solving a nonlinear equation (see the detailed information about the k-curve calibration in Section 2 in the Supporting Information). The converted conductivities of saline solutions in three sensors using both the single-point and the k-curve calibration are summarized in Figure 3c, which is the result of the AC frequency at 100 kHz. For the single-point calibration, the cell constant was determined by the measured conductance in the reference solution (0.0329 S/m), and the other measured conductance was converted into the conductivity value using the determined cell constant. Measured errors of the single-point calibration in saline solutions with conductivities of 0.0155, 0.0329, 0.0696, 0.170, 0.447, and 1.096 S/m were 50.5, −0.9, −18.3, −28.0, −32.6, and −34.8% from actual conductivity of saline solutions, respectively. In the case of the k-curve calibration, the k-curve was obtained based on the cell constants of saline solutions (σ = 0.0155–0.447 S/m), and the measured conductance was converted into the conductivity by solving the nonlinear equation, as described in Section 2 in the Supporting Information. The errors from the actual

https://dx.doi.org/10.1021/acssensors.0c00078
ACS Sens. 2020, 5, 1363−1373

conductivity of the saline solution were −0.001, −0.006, −0.02, −0.48, and −4.83%, which dramatically compensate the error comparing with the single-point calibration. However, to utilize the *k*-curve calibration, variation of the cell constant between electrical conductivity sensors should be as low as possible because several cell constants should be preobtained to get the *k*-curve for the calibration. The variation of the cell constant between three sensors is shown in Figure 3b. The variation was small enough in the frequency range over the 2 kHz, which means that the preobtained *k*-curve from a single electrical conductivity sensor can be utilized for the *k*-curve calibration of the other electrical conductivity sensor at these frequencies.

Characterization of the pH Sensor. For the sensing of pH, an IrOx layer on the Au electrode was utilized. The IrOx layer was successfully electrodeposited by cyclic voltammetry with a potential range from −0.8 to 0.7 V with respect to the Ag/AgCl reference electrode. The cyclic voltammogram during electrodeposition is shown in Figure S4, and it is similar to the previously reported cyclic voltammogram, with clear two anodic and two cathodic peaks.[38,39,44] The pH of phosphate buffer test solutions (pH 6.6−7.4) was measured by monitoring the open-circuit potential (OCP) between the fabricated IrOx layer and the screen-printed Ag/AgCl pseudo-reference electrode for 30 s. As shown in Figure 3d, there was a drift in the measured OCP for a few seconds at the start of the measurement; however, the OCP was stabilized within 10 s, showing a constant potential. The measured potential of the pH sensor in Figure 3d is shown as a gray curve in Figure 3e. The measured sensitivity in the pH range from 6.6 to 7.4 was −78.74 mV/pH with R^2 = 0.998.

Although the IrOx-based pH sensor shows a stable response, high sensitivity, and linear response to the pH, the large deviance of OCP between different sensors in the same pH solution was observed, as shown in Figure 3e. Therefore, obtaining the pH value using only the OCP value is not recommended. This deviation is usually attributed to various oxidation states of the IrOx layer shown in the cyclic voltammogram, as reported by Carroll and Baldwin's work.[44] According to this work, when the redox reaction between Ir^{3+} and Ir^{4+} is considered, the Nernst equation of the IrOx can be described as below

$$E = E^0 - 2.3RT/2F\log([Ir_2O_3]/[IrO_2]^2[H^+]^2) \quad \text{(for anhydrous)} \tag{1}$$

$$E = E^0 - 2.3RT/2F\log([Ir_2O_3]/[IrO_2]^2[H^+]^3) \quad \text{(for hydrated)} \tag{2}$$

where E^0, R, T, F, $[Ir_2O_3]$, $[IrO_2]$, and $[H^+]$ are the standard potential of the IrOx, the universal gas constant, temperature, the faraday constant, concentration of Ir_2O_3, IrO_2, and hydrogen ion, respectively. Therefore, different oxidation states inside the IrOx layer between different pH sensors can affect the sensitivity and the OCP, which is difficult to be controlled during the IrOx deposition process. The measured sensitivity of the individual sensors were −79.74, −81.55, −85.33, and −79.16 mV/pH. However, in every sensor, R^2 values were over 0.99, indicating an excellent linear response regardless of the differences of the oxidation state. Therefore, a two-point calibration process based on the OCP at pH 6.6 and 7.4 was utilized to convert the measured OCP into the pH value, as shown in Figure 3f. The calibrated pH value was almost similar to that of the pH solution, which is described as the $y = x$ line, and relative errors between average measured pH and actual pH were 0.31% (standard deviation (SD) = 0.0060), 0.55 (SD = 0.031), and 0.32% (SD = 0.015) in the pH solution with pH of 6.8, 7.0, and 7.2, respectively. Therefore, based on these results, the fabricated IrOx could show a reliable response with respect to surrounding pH changes and could be successfully utilized as a pH sensor.

Characterization of Glucose Sensor. The enzymatic glucose sensor on the microscale biosensor array was constructed based on the electropolymerization of poly(*o*-phenylenediamine) (PoPD) for the GOx immobilization on the Prussian blue-mediated carbon electrode. The principle of the glucose sensing is schematically illustrated in Figure 4a.

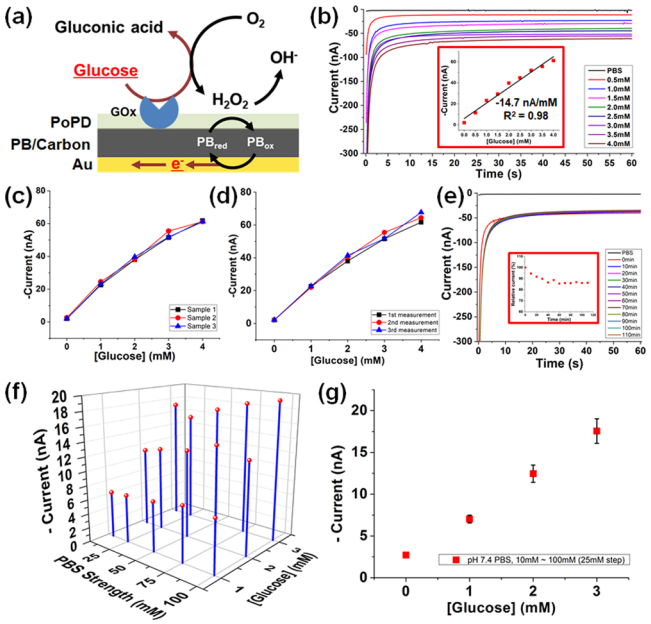

Figure 4. Characteristics of the electropolymerized PoPD-GOx-PB/carbon-based glucose sensor: (a) schematic image of the working principle of the PoPD-GOx-PB/carbon-based glucose sensor. (b) Amperograms and calibration curve of the glucose sensor in the glucose range from 0 to 4 mM. (c) Uniformity between three glucose sensors showing an average sensitivity of −14.78 nA/mM with a standard deviation of 0.059 nA/mM. (d) Calibration curves of three successive measurements in the same sensor showing an average sensitivity of −15.55 nA/mM with the standard deviation of 0.63 nA/mM. (e) Stability test with successive chronoamperometry for 2 h with an interval of 10 mins. (f) Summarized chronoamperometric currents of the glucose sensor under different ionic strengths and glucose concentrations. (g) Average currents vs glucose concentrations with diverse ionic strength conditions.

When the glucose in a surrounding medium is decomposed into gluconic acid by GOx, hydrogen peroxide (H_2O_2) is produced, as a by-product, proportionally to the glucose concentration. Then, the produced H_2O_2 can be electrochemically reduced by the reaction with Prussian blue, which is widely known as an artificial peroxidase, under low reduction potential (usually less than −0.2 V). As a result, a number of electrons in a unit time (namely, the current) generated from the above-mentioned redox process can be translated as the glucose concentration in the surrounding medium.

https://dx.doi.org/10.1021/acssensors.0c00078
ACS Sens. 2020, 5, 1363−1373

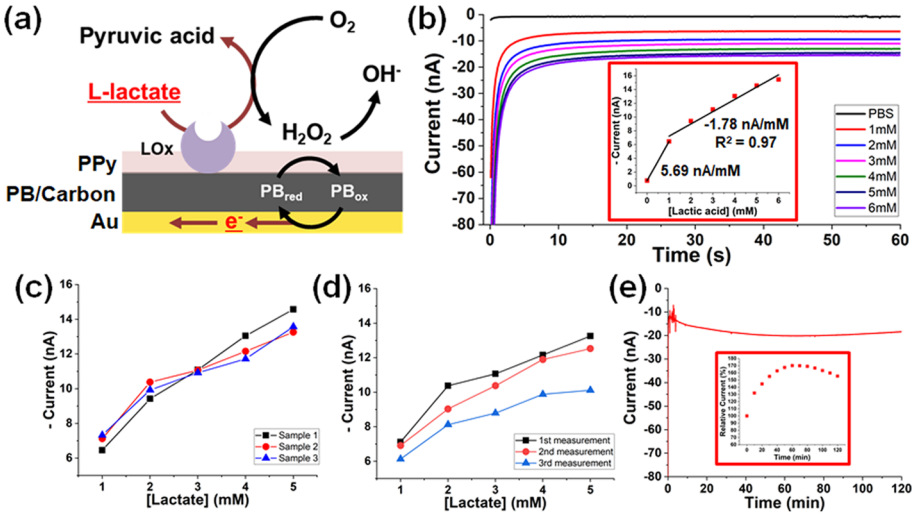

Figure 5. Characteristics of the electropolymerized PPy-LOx-PB/carbon-based lactate sensor: (a) schematic image of the working principle of the PPy-LOx-PB/carbon-based lactate sensor. (b) Amperograms and calibration curve of the lactate sensor in the lactate range from 0 to 6 mM. (c) Uniformity between three lactate sensors and (d) calibration curves for three successive measurements by the same sensor. (e) Stability test of the lactate sensor by measuring the chronoamperometric current for 2 h.

Chronoamperometric measurements were performed to characterize the fabricated glucose sensor. Amperograms we recorded for the glucose concentrations from 0 to 4 mM for 60 s under a redox potential of −0.2 V with respect to the Ag/AgCl pseudo-reference electrode. As shown in Figure 4b, the chronoamperometric current increased linearly with the increase in glucose concentration, and the measured sensitivity of the sensor was −14.7 nA/mM with an R^2 value of 0.98. Sensor reproducibility was studied between three glucose sensors, which were fabricated using biosensors from the same batch and the same oPD-GOx electropolymerization solution. The calibration curves of these three glucose sensors are summarized in Figure 4c. All three sensors showed a similar chronoamperometric current for the same glucose concentrations. The measured average sensitivity of the three sensors was −14.78 nA/mM (averaged R^2 = 0.98) with a SD of 0.059 nA/mM, showing that the fabricated sensors have an excellent uniformity. Furthermore, successive calibrations for the same sensor were performed to investigate the repeatability of the sensor. After one measurement, the glucose sensor was thoroughly rinsed with PBS to remove any remaining glucose on the sensor for the next measurement. Figure 4d shows the summary of the calibration curves for the repeated measurements, showing that the chronoamperometric currents for the same glucose concentration were similar. Since the GOx was successfully immobilized on the carbon electrode by the electropolymerized PoPD membrane, and such immobilization was robust, the enzyme activity of the GOx was stable for several measurement cycles. For the three calibration curves, the measured averaged sensitivity was −15.55 nA/mM (averaged R^2 = 0.98), and the average SD was 0.63 nA/mM. The stability of the glucose sensor was also investigated by performing repeated chronoamperometry (total of 11 times) for the same glucose solution ([glucose] = 2 mM) with an interval of 10 min. Within 40 min after the initial chronoamperometry, the chronoamperometric current continuously decreased up to 86.5% of the first chronoamperometric current, as shown in Figure 4e. However, the chronoamperometric current was soon stabilized with a similar relative current of 85%.

In the case of chronoamperometric sensors, the current response can be affected by the resistance of the supporting medium (electrolyte). Normally, this effect is not considered as a significant problem in conventional measurements because homogeneous media, such as PBS or blood, with a constant conductivity are typically used in the glucose analysis. However, when there is a difference in the conductivity at the sensor environment, such as the type of tissue being normal or cancerous, the characteristics of the glucose sensor can be altered due to the above-mentioned effect. Therefore, chronoamperometric currents of the glucose sensor in PBS with various ionic strengths (i.e., different conductivities) were investigated. Figure 4f,g shows the measured chronoamperometric current at 60 s, according to the different ionic strength of PBS and different glucose concentrations. Here, it is clearly observed that the effect of glucose concentrations to the chronoamperometric current is much higher than that of the ionic strength. The averaged chronoamperometric current for the glucose concentrations of 1, 2, and 3 mM were −7.02 (SD = 0.47 nA), −12.46 (1.03 nA), and −17.56 nA (1.47 nA), respectively. This result confirms that the chronoamperometric current is mostly governed by the glucose concentration, while the effect of conductivity of the supporting medium is not significant.

Characterization of Lactate Sensor. The enzymatic lactate sensor was constructed with a similar principle and configuration as the glucose sensor. For the active layer of the lactate sensor, the Prussian blue-mediated carbon electrode transducer was functionalized by entrapping LOx within an electropolymerized poly(pyrrole) film. The principle of the enzymatic lactate sensor is illustrated in Figure 5a. Lactic acid (L-lactate) is enzymatically decomposed into pyruvic acid by LOx, generating H_2O_2, as a by-product, proportionally to the lactic acid concentration. The generated H_2O_2 is then electrochemically reduced with the oxidation of Prussian blue in the carbon electrode. The measured current from the reduction of Prussian blue, under low reduction potential (less than −0.2 V), is proportional to the lactate concentration in the surrounding medium.

https://dx.doi.org/10.1021/acssensors.0c00078
ACS Sens. 2020, 5, 1363−1373

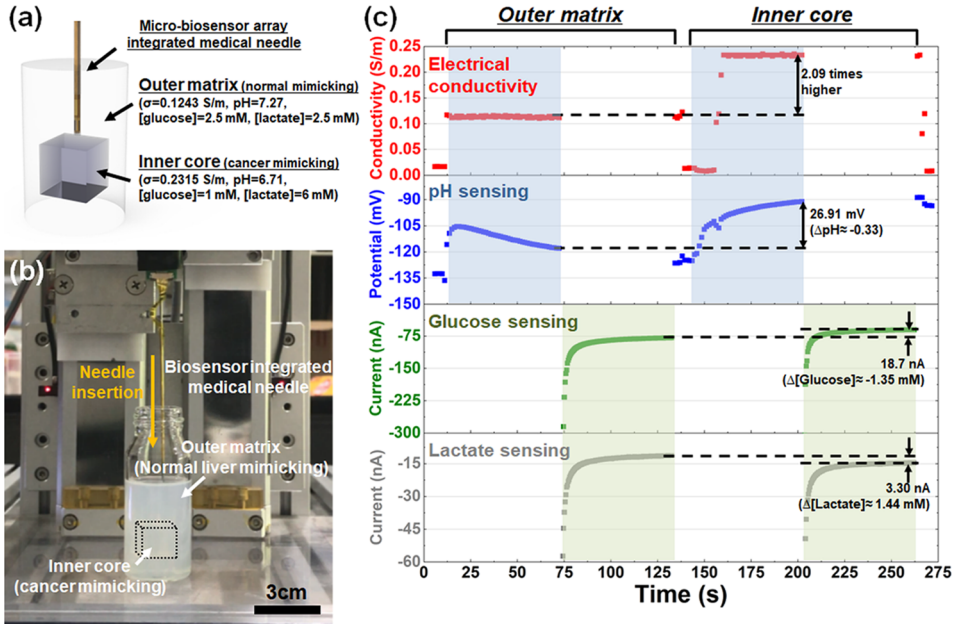

Figure 6. Demonstration of a real-time multiparameter measurement using the cancer environment-mimicking hydrogel phantom: (a) schematics of the prepared hydrogel phantom with the outer matrix (mimicking the normal tissue) and the inner core (mimicking the cancerous tissue) and (b) photograph image of the actual experimental setup. (c) Graph of the measured multiparameters (electrical conductivity, pH, glucose, and lactate) during needle insertion. First, the medical needle integrated with a microscale biosensor array was placed at the outer matrix and the electrical conductivity and pH were measured for 1 min. Then, the chronoamperometry sensing of glucose and lactate was performed for 1 min. After the measurement at the outer matrix, the needle was further inserted to the inner core and the measurement was performed by the same process used for the outer matrix.

To immobilize the LOx on the carbon electrode, we utilized electropolymerized PPy instead of the PoPD to improve the limited linear range. For most lactate sensing applications, such as sweat analysis,[3,45−49] a wide linear range, up to several tens of molarity, is usually required. However, the Michaelis−Menten constant of the commercially available LOx, determined as the substrate concentration when the reaction velocity is half of the maximum reaction velocity, is usually less than 1 mM. This means that the LOx-based lactate sensor saturates at low lactate concentrations, which is not appropriated in applications that demands the detection of high lactate concentration. Therefore, an additional functional layer, such as a porous polymeric membrane, Nafion, or hydrogels, must be utilized to limit the diffusion process of lactate and widen the linear range of the lactate sensor.[17,50,51] However, in the case of lactate sensor realized by immobilizing LOx via electropolymerization, forming an additional effective diffusion-limiting layer is difficult, and most of previous reports have suffered from limited linear range (<2 mM).[52] Furthermore, it is known that the PoPD layer has high diffusivity of small molecules such as H_2O_2 through the layer; therefore, the use of the PoPD layer for the lactate sensor does not play an effective role as a diffusion-limiting layer.[53] On the other hand, in the case of PPy, it has been reported that the electropolymerized PPy membrane with a low monomer (Py) concentration, about 5 mM, can have a densely packed structure; therefore, the diffusion process of ions through the membrane was found to be significantly reduced.[54] Based on the above-mentioned facts, we utilized a PPy membrane with a low monomer concentration ([Py] = 4 mM) for the LOx enzyme immobilization to realize a lactate sensor with a linear range of up to 6 mM (see the detailed optimized electropolymerization parameters for the PPy-LOx-based lactate sensor in Section 3 in the Supporting Information).

The chronoamperometry response of the lactate sensor is shown in Figure 5b. The chronoamperometric current tends to be saturated by increased lactate concentration; however, it shows a moderately linear response of up to 6 mM of the lactate concentration, which is a markedly enhanced linear range comparing to previously reported electropolymerization-based lactate sensors.[52] The measured sensitivity in the lactate concentration ranging from 0 to 1 mM and from 1 to 6 mM were −5.70 and −1.78 nA/mM (R^2 of 0.97), respectively. In the case of the uniformity between sensors, as shown in Figure 5c, the deviation in the chronoamperometric currents for the same lactate concentrations was larger than that for the glucose sensor. However, it still shows similar sensitivities between the sensors with an average of −1.62 nA/mM and a SD of −0.25 nA/mM. Opposed to the glucose sensor, the lactate sensor does not show good repeatability for multiple measurement cycles (Figure 5d), which can be attributed to the detachment of the LOx from the electropolymerized PPy layer. This problem can be attributed to the densely packed but sand-like structure of the PPy film. It is expected to be resolved by forming an additional immobilization layer such as the PoPD layer on the top of the PPy-LOx film. To investigate the stability of the lactate sensor, the chronoamperometric current was continuously measured for 2 h, as shown in Figure 5e. The measured chronoamperometric current tends to increase up to 170% within 1 h from its initial measurement and then decreased to 155%. In brief, the fabricated LOx-based lactate sensor shows relatively unstable response under repeated and long-time measurement, notwithstanding that it still has moderate sensitivity and linear range. Therefore, the sensor can be utilized in single-time measurement applications with a

https://dx.doi.org/10.1021/acssensors.0c00078
ACS Sens. 2020, 5, 1363−1373

short measurement period, such as a local lactate concentration measurement inside the tissue.

Real-Time Multiparameter Sensing in Hydrogel Phantom. To demonstrate the capability of multiparameter sensing, a hydrogel phantom consisting of an inner core and outer matrix to mimic the cancerous and normal tissue environments, respectively, was utilized as a sample (Figure 6a). The needle-based sensor array aims at providing real-time tissue discrimination of glucose, lactate, pH and electrical conductivity changes associated with the cancer-specific metabolic process. The prepared microbiosensor array integrated medical needle was inserted through the hydrogel phantom (Figure 6b), and the electrical conductivity, pH, glucose concentration, and lactate concentration in the outer matrix and in the inner core were measured, sequentially. During the needle insertion, the electrical conductivity and pH were measured for 1 min, and then, the chronoamperometry measurements of both glucose and lactate sensors were performed for 1 min, simultaneously. The graph in Figure 6c shows the measured multiparameters during the needle insertion (see also Video S1 for the experimental process of the real-time multiparameter sensing). When the needle was in the outer matrix, the measured electrical conductivity and potential of the pH sensor were 0.11 S/m and −118.03 mV, respectively. After the electrical conductivity and pH measurements, the chronoamperometry was performed in the glucose and lactate sensors, and the measured chronoamperometric currents were −79.33 and −1.44 nA, respectively. Then, the needle was further inserted into the inner core and the same protocol was carried out. It should be noted that Parafilm, which was used to passivate between the inner core and outer matrix to prevent the diffusion of ions, temporarily blocked the electrical conductivity sensor during the needle penetration into the core (between 140 and 160 s in Figure 6c). Because of this problem, the needle was pulled out and reinserted into the inner core directly. At the inner core, the measurement was carried out with the same procedure as the outer matrix, and the measured electrical conductivity and potential at the pH sensor were 0.23 S/m and −91.12 mV, respectively, while the measured chronoamperometric currents for the glucose and lactate sensors were −60.62 and −14.73 nA, respectively. In the case of the electrical conductivity sensor, the measured electrical conductivities at both outer matrix (0.11 S/m) and inner core (0.23 S/m) were almost identical with the actual electrical conductivity of PBS at both the outer matrix (0.1243 S/m) and the inner core (0.2315 S/m). The measured pH difference between the outer matrix and the inner core was about −0.36, while the actual difference was −0.56. In the case of the glucose sensor, the measured difference of the glucose concentration was −1.27 mM, while the real difference was −1.5 mM. The difference of the lactate concentration was 1.85 mM, which has a large deviation from the actual difference of 3.5 mM. There may be several reasons for the difference between the measured and the actual value of parameters. First of all, the ions of both the inner core and the outer matrix could be diffused when the needle penetrated the passivation layer (i.e., Parafilm). Furthermore, there can be a difference in the sensitivity between sensor batches, although a reasonable uniformity has been verified for the same batch in the sensor characterization. In the case of the lactate sensor, which shows a relatively larger error, the immobilized LOx may be detached from the electrode as described in the characterization part of the lactate sensor. However, in this demonstration, besides the challenges faced, the fabricated needle integrated with the multiplexed microbiosensor array was able to discriminate nonhomogeneous environments. Therefore, it can be potentially utilized as a probe for the in vivo tissue discrimination in the future. For the real medical applications, we expect that the boundary between different tissues can be rapidly recognized using the change of the electrical conductivity and pH with the advantage of their short measurement times and fast sensor responses. After the boundary is determined, additional analysis can be performed by multiparametric measurement using other electrochemical sensors (i.e., glucose and lactate sensors), which need more time to measure parameters.

CONCLUSIONS

In this research, we report the microscale biosensor array on a flexible polyimide substrate and its application by integrating the sensor array onto a medical needle for real-time multiparametric sensing toward a lab-on-a-needle system. The microscale biosensor array presents the capability of multiparametric determination of electrical conductivity, pH, glucose concentration, and lactate concentration. The microscale sensor array was fabricated on the polyimide film using the micropatterning methods, and it was thin enough to be attached onto the curved surface of the needle. Then, various active materials for the electrochemical sensing were selectively formed on the surface of the sensor electrodes using the electrodeposition method. Based on this fabrication method, three electrochemical sensors (targeting pH, glucose, and lactate) were successfully integrated within an area of 2 mm × 2 mm, and four sensors for multiparametric bioassay were totally integrated within an area of 2 mm × 5 mm. The performance and characteristics of each sensor were quantitatively analyzed using solution samples with analytes, and the needed calibration methods for reliable measurement were suggested and demonstrated. The feasibility of real-time multiparametric sensing using the sensor integrated medical needle during the needle insertion was further demonstrated with a hydrogel phantom, which mimicked the normal and cancerous tissues. The differences of multiparameters between the cancer-mimicking (inner core) and normal-tissue mimicking part (outer matrix) were successfully measured.

The sensor integrated medical devices for in vivo sensing with a minimally invasive manner will get more attention because of the need for early prediction and treatment of various diseases. The new advanced method for the fabricating microscale biosensor array and integration onto the curved surface (i.e., the medical needle) addresses current major limitations of the fabrication and integration of advanced sensors onto the medical tools. Furthermore, other types of sensors, such as an aptamer-based sensor for biomarker detection or optical sensor for in vivo fluorescence imaging, could be similarly realized through, hence extending the boundary of in vivo sensing for early prediction and monitoring of diseases.

ASSOCIATED CONTENT

Supporting Information

The Supporting Information is available free of charge at https://pubs.acs.org/doi/10.1021/acssensors.0c00078.

Schematic illustration of the cancer microenvironment, schematic image of the fabrication process, experimental setup of the real-time multiparametric measurement,

https://dx.doi.org/10.1021/acssensors.0c00078
ACS Sens. 2020, 5, 1363−1373

cyclic voltammogram of IrOx electrodeposition, description of the cell constant, the description of the *k*-curve calibration, and optimization of electropolymerized parameters for the PPy-LOx lactate sensor (PDF)
Video showing the experimental process of real-time multiparameter sensing in the hydrogel phantom (AVI)

AUTHOR INFORMATION

Corresponding Authors

Joseph Wang − *Department of NanoEngineering, University of California, San Diego, La Jolla, California 92093, United States;* orcid.org/0000-0002-4921-9674; Email: josephwang@ucsd.edu

Inkyu Park − *Department of Mechanical Engineering, Korea Advanced Institute of Science and Technology (KAIST), Daejeon 34141, South Korea;* orcid.org/0000-0001-5761-7739; Email: inkyu@kaist.ac.kr

Authors

Jaeho Park − *Department of Mechanical Engineering, Korea Advanced Institute of Science and Technology (KAIST), Daejeon 34141, South Korea*

Juliane R. Sempionatto − *Department of NanoEngineering, University of California, San Diego, La Jolla, California 92093, United States*

Jayoung Kim − *Department of NanoEngineering, University of California, San Diego, La Jolla, California 92093, United States*

Yongrok Jeong − *Department of Mechanical Engineering, Korea Advanced Institute of Science and Technology (KAIST), Daejeon 34141, South Korea*

Jimin Gu − *Department of Mechanical Engineering, Korea Advanced Institute of Science and Technology (KAIST), Daejeon 34141, South Korea*

Complete contact information is available at: https://pubs.acs.org/10.1021/acssensors.0c00078

Author Contributions

[§]J.P., J.R.S., J.W., and I.P. contributed equally to this work.

Notes

The authors declare no competing financial interest.

ACKNOWLEDGMENTS

This work was supported by the National Research Foundation of Korea (NRF) grant funded by the Korean government (MSIT) (no. 2018R1A2B2004910).

REFERENCES

(1) Clark, L. C., Jr.; Lyons, C. Electrode Systems for Continuous Monitoring in Cardiovascular Surgery. *Ann. N. Y. Acad. Sci.* **1962**, *102*, 29−45.

(2) Kim, J.; Campbell, A. S.; de Ávila, B. E. F.; Wang, J. Wearable Biosensors for Healthcare Monitoring. *Nat. Biotechnol.* **2019**, *37*, 389−406.

(3) Gao, W.; Emaminejad, S.; Nyein, H. Y. Y.; Challa, S.; Chen, K.; Peck, A.; Fahad, H. M.; Ota, H.; Shiraki, H.; Kiriya, D.; et al. Fully Integrated Wearable Sensor Arrays for Multiplexed in Situ Perspiration Analysis. *Nature* **2016**, *529*, 509−514.

(4) Yang, Y.; Song, Y.; Bo, X.; Min, J.; Pak, O. S.; Zhu, L.; Wang, M.; Tu, J.; Kogan, A.; Zhang, H.; et al. A Laser-Engraved Wearable Sensor for Sensitive Detection of Uric Acid and Tyrosine in Sweat. *Nat. Biotechnol.* **2020**, 217−224.

(5) Lee, H.; Choi, T. K.; Lee, Y. B.; Cho, H. R.; Ghaffari, R.; Wang, L.; Choi, H. J.; Chung, T. D.; Lu, N.; Hyeon, T.; et al. A Graphene-Based Electrochemical Device with Thermoresponsive Microneedles for Diabetes Monitoring and Therapy. *Nat. Nanotechnol.* **2016**, *11*, 566−572.

(6) Xiang, Z.; Wang, H.; Pastorin, G.; Lee, C. Development of a Flexible and Disposable Microneedle-Fluidic-System with Finger-Driven Drug Loading and Delivery Functions for Inflammation Treatment. *J. Microelectromech. Syst.* **2015**, *24*, 565−574.

(7) Wang, H.; Pastorin, G.; Lee, C. Toward Self-Powered Wearable Adhesive Skin Patch with Bendable Microneedle Array for Transdermal Drug Delivery. *Adv. Sci.* **2016**, *3*, 1500441.

(8) Park, J.; Jeong, Y.; Kim, J.; Gu, J.; Wang, J.; Park, I. Biopsy Needle Integrated with Multi-Modal Physical/Chemical Sensor Array. *Biosens. Bioelectron.* **2020**, *148*, 111822.

(9) Arroyo-Currás, N.; Somerson, J.; Vieira, P. A.; Ploense, K. L.; Kippin, T. E.; Plaxco, K. W. Real-Time Measurement of Small Molecules Directly in Awake, Ambulatory Animals. *Proc. Natl. Acad. Sci. U. S. A.* **2017**, *114*, 645−650.

(10) Lee, H.; Lee, Y.; Song, C.; Cho, H. R.; Ghaffari, R.; Choi, T. K.; Kim, K. H.; Lee, Y. B.; Ling, D.; Lee, H.; et al. An Endoscope with Integrated Transparent Bioelectronics and Theranostic Nanoparticles for Colon Cancer Treatment. *Nat. Commun.* **2015**, *6*, 10059.

(11) Tian, L.; Wang, H.; Yu, X.; Silva, A. C.; Yu, Y.; Koh, A.; Oklu, R.; Chempakasseril, A.; Albadawi, H.; Yuan, J.; et al. Needle-Shaped Ultrathin Piezoelectric Microsystem for Guided Tissue Targeting via Mechanical Sensing. *Nat. Biomed. Eng.* **2018**, 165.

(12) Yun, J.; Kang, G.; Park, Y.; Kim, H. W.; Cha, J. J.; Lee, J. H. Electrochemical Impedance Spectroscopy with Interdigitated Electrodes at the End of Hypodermic Needle for Depth Profiling of Biotissues. *Sens. Actuators, B* **2016**, *237*, 984−991.

(13) Li, T.; Gianchandani, R. Y.; Gianchandani, Y. B. Micromachined Bulk PZT Tissue Contrast Sensor for Fine Needle Aspiration Biopsy. *Lab Chip* **2007**, *7*, 179−185.

(14) Fang, Y.; Wang, S.; Liu, Y.; Xu, Z.; Zhang, K.; Guo, Y. Development of Cu Nanoflowers Modified the Flexible Needle-Type Microelectrode and Its Application in Continuous Monitoring Glucose in Vivo. *Biosens. Bioelectron.* **2018**, *110*, 44−51.

(15) Russell, C.; Ward, A. C.; Vezza, V.; Hoskisson, P.; Alcorn, D.; Steenson, D. P.; Corrigan, D. K. Development of a Needle Shaped Microelectrode for Electrochemical Detection of the Sepsis Biomarker Interleukin-6 (IL-6) in Real Time. *Biosens. Bioelectron.* **2019**, *126*, 806−814.

(16) Fang, L.; Liang, B.; Yang, G.; Hu, Y.; Zhu, Q.; Ye, X. A Needle-Type Glucose Biosensor Based on PANI Nanofibers and PU/E-PU Membrane for Long-Term Invasive Continuous Monitoring. *Biosens. Bioelectron.* **2017**, *97*, 196−202.

(17) Yang, Q.; Atanasov, P.; Wilkins, E. An Integrated Needle-Type Biosensor for Intravascular Glucose and Lactate Monitoring. *Electroanalysis* **1998**, *10*, 752−757.

(18) Kim, S.; Park, J.-H.; Kang, K.; Park, C.-O.; Park, I. Direct Metal Micropatterning on Needle-Type Structures towards Bioimpedance and Chemical Sensing Applications. *J. Micromech. Microeng.* **2015**, *25*, No. 015002.

(19) Du, X.; Durgan, C. J.; Matthews, D. J.; Motley, J. R.; Tan, X.; Pholsena, K.; Árnadóttir, L.; Castle, J. R.; Jacobs, P. G.; Cargill, R. S.; et al. Fabrication of a Flexible Amperometric Glucose Sensor Using Additive Processes. *ECS J. Solid State Sci. Technol.* **2015**, *4*, P3069−P3074.

(20) Bharati, S.; Rishi, P.; Tripathi, S. K.; Koul, A. Changes in the Electrical Properties at an Early Stage of Mouse Liver Carcinogenesis. *Bioelectromagnetics* **2013**, *34*, 429−436.

(21) Heileman, K.; Daoud, J.; Tabrizian, M. Dielectric Spectroscopy as a Viable Biosensing Tool for Cell and Tissue Characterization and Analysis. *Biosens. Bioelectron.* **2013**, *49*, 348−359.

(22) Song, C. W.; Griffin, R.; Park, H. J. Influence of Tumor PH on Therapeutic Response. *Cancer Drug Resist.* **2006**, 21−42.

(23) Estrella, V.; Chen, T.; Lloyd, M.; Wojtkowiak, J.; Cornnell, H. H.; Ibrahim-Hashim, A.; Bailey, K.; Balagurunathan, Y.; Rothberg, J. M.; Sloane, B. F.; et al. Acidity Generated by the Tumor Microenvironment Drives Local Invasion. *Cancer Res.* **2013**, *73*, 1524−1535.

(24) Helmlinger, G.; Yuan, F.; Dellian, M.; Jain, R. K. Interstitial PH and PO_2 Gradients in Solid Tumors in Vivo: High-Resolution Measurements Reveal a Lack of Correlation. *Nat. Med.* **1997**, *3*, 177−182.
(25) Liberti, M. V.; Locasale, J. W. The Warburg Effect: How Does It Benefit Cancer Cells? *Trends Biochem. Sci.* **2016**, *41*, 211−218.
(26) Walenta, S.; Chau, T.-V.; Schroeder, T.; Lehr, H.-A.; Kunz-Schughart, L. A.; Fuerst, A.; Mueller-Klieser, W. Metabolic Classification of Human Rectal Adenocarcinomas: A Novel Guideline for Clinical Oncologists? *J. Cancer Res. Clin. Oncol.* **2003**, *129*, 321−326.
(27) Hirayama, A.; Kami, K.; Sugimoto, M.; Sugawara, M.; Toki, N.; Onozuka, H.; Kinoshita, T.; Saito, N.; Ochiai, A.; Tomita, M.; et al. Quantitative Metabolome Profiling of Colon and Stomach Cancer Microenvironment by Capillary Electrophoresis Time-of-Flight Mass Spectrometry. *Cancer Res.* **2009**, *69*, 4918−4925.
(28) Vander Heiden, M. G.; Cantley, L. C.; Thompson, C. B.; Mammalian, P.; Exhibit, C.; Metabolism, A. Understanding the Warburg Effect : Cell Proliferation. *Science* **2009**, *324*, 1029.
(29) Kimura, S.; Morimoto, T.; Uyama, T.; Monden, Y.; Kinouchi, Y.; Iritani, T. Application of Electrical Impedance Analysis for Diagnosis of a Pulmonary Mass. *Chest* **1994**, *105*, 1679−1682.
(30) Surowiec, A. J.; Stuchly, S. S.; Barr, J. R.; Swarup, A. Dielectric Properties of Breast Carcinoma and the Surrounding Tissues. *IEEE Trans. Biomed. Eng.* **1988**, *35*, 257−263.
(31) Aberg, P.; Nicander, I.; Hansson, J.; Geladi, P.; Holmgren, U.; Ollmar, S. Skin Cancer Identification Using Multifrequency Electrical Impedance–a Potential Screening Tool. *IEEE Trans. Biomed. Eng.* **2004**, *51*, 2097−2102.
(32) da Silva, J. E.; de Sá, J. P. M.; Jossinet, J. Classification of Breast Tissue by Electrical Impedance Spectroscopy. *Med. Biol. Eng. Comput.* **2000**, *38*, 26−30.
(33) Haemmerich, D.; Staelin, S. T.; Tsai, J. Z.; Tungjitkusolmun, S.; Mahvi, D. M.; Webster, J. G. In Vivo Electrical Conductivity of Hepatic Tumours. *Physiol. Meas.* **2003**, *24*, 251−260.
(34) Laufer, S.; Ivorra, A.; Reuter, V. E.; Rubinsky, B.; Solomon, S. B. Electrical Impedance Characterization of Normal and Cancerous Human Hepatic Tissue. *Physiol. Meas.* **2010**, *31*, 995−1009.
(35) Halter, R. J.; Schned, A.; Heaney, J.; Hartov, A.; Paulsen, K. D. Electrical Properties of Prostatic Tissues: I. Single Frequency Admittivity Properties. *J. Urol.* **2009**, *182*, 1600−1607.
(36) Kato, Y.; Ozawa, S.; Miyamoto, C.; Maehata, Y.; Suzuki, A.; Maeda, T.; Baba, Y. Acidic Extracellular Microenvironment and Cancer. *Cancer Cell Int.* **2013**, *13*, 89.
(37) Huang, W. D.; Cao, H.; Deb, S.; Chiao, M.; Chiao, J. C. A Flexible PH Sensor Based on the Iridium Oxide Sensing Film. *Sens. Actuators, A* **2011**, *169*, 1−11.
(38) Kakooei, S.; Ismail, C.; Ari-Wahjoedi, B. An Overview of PH Sensors Based on Iridium Oxide: Fabrication and Application. *Int. J. Mater. Sci. Innovations* **2013**, *1*, 62−72.
(39) Yamanaka, K. Anodically Electrodeposited Iridium Oxide Films (AEIROF) from Alkaline Solutions for Electrochromic Display Devices. *Jpn. J. Appl. Phys.* **1989**, *28*, 632−637.
(40) Gabriel, C.; Gabriel, S.; Corthout, E. The Dielectric Properties of Biological Tissues: I. Literature Survey. *Phys. Med. Biol.* **1996**, *41*, 2231−2249.
(41) Gabriel, C.; Peyman, A.; Grant, E. H. Electrical Conductivity of Tissue at Frequencies below 1 MHz. *Phys. Med. Biol.* **2009**, *54*, 4863−4878.
(42) Gabriel, S.; Lau, R. W.; Gabriel, C. The Dielectric Properties of Biological Tissues: III. Parametric Models for the Dielectric Spectrum of Tissues. *Phys. Med. Biol.* **1996**, *41*, 2271−2293.
(43) Park, J.; Choi, W.-M.; Kim, K.; Jeong, W.-I.; Seo, J.-B.; Park, I. Biopsy Needle Integrated with Electrical Impedance Sensing Micro-electrode Array towards Real-Time Needle Guidance and Tissue Discrimination. *Sci. Rep.* **2018**, *8*, 264.
(44) Carroll, S.; Baldwin, R. P. Self-Calibrating Microfabricated Iridium Oxide PH Electrode Array for Remote Monitoring. *Anal. Chem.* **2010**, *82*, 878−885.
(45) Alam, F.; RoyChoudhury, S.; Jalal, A. H.; Umasankar, Y.; Forouzanfar, S.; Akter, N.; Bhansali, S.; Pala, N. Lactate Biosensing: The Emerging Point-of-Care and Personal Health Monitoring. *Biosens. Bioelectron.* **2018**, *117*, 818−829.
(46) Anastasova, S.; Crewther, B.; Bembnowicz, P.; Curto, V.; Ip, H. M.; Rosa, B.; Yang, G. Z. A Wearable Multisensing Patch for Continuous Sweat Monitoring. *Biosens. Bioelectron.* **2017**, *93*, 139−145.
(47) Bandodkar, A. J.; Gutruf, P.; Choi, J.; Lee, K. H.; Sekine, Y.; Reeder, J. T.; Jeang, W. J.; Aranyosi, A. J.; Lee, S. P.; Model, J. B.; et al. Battery-Free, Skin-Interfaced Microfluidic/Electronic Systems for Simultaneous Electrochemical, Colorimetric, and Volumetric Analysis of Sweat. *Sci. Adv.* **2019**, *5*, No. eaav3294.
(48) Derbyshire, P. J.; Barr, H.; Davis, F.; Higson, S. P. J. Lactate in Human Sweat: A Critical Review of Research to the Present Day. *J. Physiol. Sci.* **2012**, *62*, 429−440.
(49) Imani, S.; Bandodkar, A. J.; Mohan, A. M. V.; Kumar, R.; Yu, S.; Wang, J.; Mercier, P. P. A Wearable Chemical-Electrophysiological Hybrid Biosensing System for Real-Time Health and Fitness Monitoring. *Nat. Commun.* **2016**, *7*, 11650.
(50) Khan, G. F.; Wernet, W. Design of Enzyme Electrodes for Extended Use and Storage Life. *Anal. Chem.* **1997**, *69*, 2682−2687.
(51) Sung, W. J.; Bae, Y. H. Glucose Oxidase, Lactate Oxidase, and Galactose Oxidase Enzyme Electrode Based on Polypyrrole with Polyanion/PEG/Enzyme Conjugate Dopant. *Sens. Actuators, B* **2006**, *114*, 164−169.
(52) Rathee, K.; Dhull, V.; Dhull, R.; Singh, S. Biosensors Based on Electrochemical Lactate Detection: A Comprehensive Review. *Biochem. Biophys. Rep.* **2016**, *5*, 35−54.
(53) Murphy, L. J. Reduction of Interference Response at a Hydrogen Peroxide Detecting Electrode Using Electropolymerized Films of Substituted Naphthalenes. *Anal. Chem.* **1998**, *70*, 2928−2935.
(54) Kulandaivalu, S.; Zainal, Z.; Sulaiman, Y. Influence of Monomer Concentration on the Morphologies and Electrochemical Properties of PEDOT, PANI, and PPy Prepared from Aqueous Solution. *Int. J. Polym. Sci.* **2016**, *2016*, 1−12.

https://dx.doi.org/10.1021/acssensors.0c00078
ACS Sens. 2020, 5, 1363−1373